Journal of Materials Chemistry C

ROYAL SOCIETY OF CHEMISTRY

PAPER

View Article Online
View Journal | View Issue

Cite this: J. Mater. Chem. C, 2025, 13, 1812

Structural frustration effects by mixed alkali ions in ferroelectric Dion–Jacobson layered perovskites (Cs,Rb)$NdNb_2O_7$†

Zhen-Tao Lu, [a] Sota Asaki,[a] Suguru Yoshida, [b] Chikako Moriyoshi, [c] George Hasegawa, [e] Koji Fujita, [d] Venkatraman Gopalan, [b] Katsuro Hayashi [a] and Hirofumi Akamatsu *[a]

Two Dion–Jacobson (DJ) double-layered perovskites $CsNdNb_2O_7$ and $RbNdNb_2O_7$ exhibit hybrid improper ferroelectricity, in which spontaneous polarization is induced by coupling of two types of nonpolar oxygen octahedral rotations (OORs). Their crystal structures adopt common polar distortion modes, although they exhibit distinct OOR patterns. In this study, complete solid-solution $Cs_{1-x}Rb_x$-$NdNb_2O_7$ ceramics (x = 0, 0.25, 0.5, 0.75, and 1) have been synthesized by conventional solid-state reaction methods, and the temperature-composition phase diagram has been established by various methods including variable-temperature synchrotron X-ray diffractometry, differential scanning calorimetry, optical second harmonic generation, and dielectric permittivity measurements. The powder X-ray diffractometry reveals that Cs-rich compounds ($x \leq 0.25$) crystalize into polar $P2_1am$ structures with $a^-a^-c^+/a^-a^-c^+$ OORs at room temperature, while Rb-rich compounds ($x \geq 0.5$) adopt polar $I2cm$ structures with $a^-a^-c^+/-(a^-a^-c^+)$ OORs. All the solid solutions exhibit ferroelectricity at room temperature. Upon heating, successive phase transitions involving the loss of polar distortions and OORs have been observed. The phase transition temperatures of the solid solutions with intermediate compositions are lower than those predicted based on Vegard's law, indicating structural frustration effects due to the random arrangement of two alkali metal ions. This work provides insight into the influence of alkali metal ions in the intervening layers on the structural and ferroelectric properties of DJ layered perovskites.

Received 30th September 2024,
Accepted 24th November 2024

DOI: 10.1039/d4tc04190a

rsc.li/materials-c

Introduction

Noncentrosymmetric materials have distinctive functional properties such as second-order nonlinear optical effects,[1,2] ferroelectricity,[3,4] pyroelectricity,[5,6] and piezoelectricity.[7,8] Ferroelectric materials have garnered significant interest for their fundamental physics due to their switchable spontaneous polarization under external fields.[9–11] They can be widely applied in non-volatile memory,[12] solar cells,[13] photocatalysts,[14] and solid-state refrigeration.[15] However, widely used commercial ferroelectric materials such as $Pb(Zr,Ti)O_3$[16,17] and $(Pb,La)(Zr,Ti)O_3$[18,19] include highly toxic lead, which damages human health and pollutes the environment. Thus, urgent efforts are needed to develop novel lead-free ferroelectric materials to replace current commercial lead-containing materials, ensuring the advancement of various applications while mitigating environmental and health concerns.

Simple perovskite oxides have a chemical formula of ABO_3, where the A-site cations are usually large cations such as alkali, alkaline earth, and rare earth cations as well as Pb^{2+} and Bi^{3+}, while the octahedrally coordinated B sites are typically occupied by small cations including transition metal ions. Most perovskite oxides crystallize in centrosymmetric structures, which conflict with the requirements for ferroelectric materials. Noncentrosymmetric perovskites account just for ~0.4% of all perovskites in the Inorganic Crystal Structure Database (ICSD), indicating a great challenge to find novel ferroelectric perovskites.[20] However, the discovery of hybrid improper

[a] Department of Applied Chemistry, Kyushu University, Motooka, Fukuoka 819-0395, Japan. E-mail: h.akamatsu@cstf.kyushu-u.ac.jp
[b] Materials Research Institute and Department of Materials Science, Pennsylvania State University, University Park, Pennsylvania 16802, USA
[c] Graduate School of Advanced Science and Engineering, Hiroshima University, Higashihiroshima, Hiroshima 739-8526, Japan
[d] Department of Material Chemistry, Kyoto University, Nishikyo, Kyoto 615-8510, Japan
[e] Institute of Materials and Systems for Sustainability, Nagoya University, Nagoya 464-8601, Japan

† Electronic supplementary information (ESI) available. See DOI: https://doi.org/10.1039/d4tc04190a

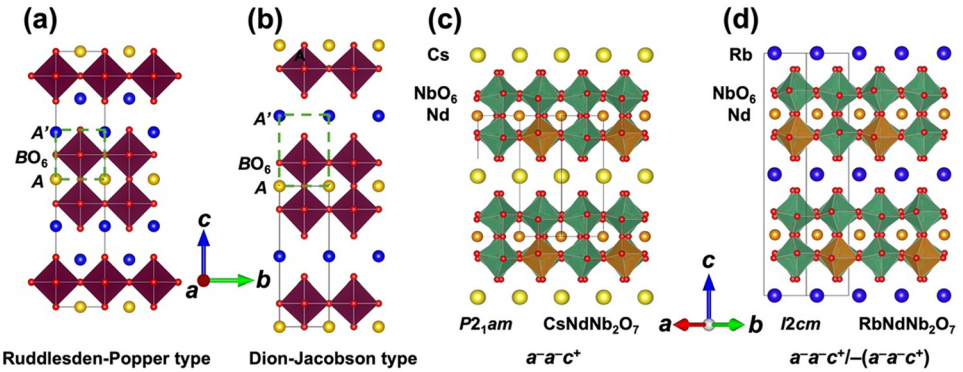

Fig. 1 Schematic crystal structures for (a) aristotype Ruddlesden–Popper and (b) Dion–Jacobson-type double-layered perovskites. Room-temperature crystal structures of (c) $CsNdNb_2O_7$ (space group: $P2_1am$) and (d) $RbNdNb_2O_7$ (space group: $I2cm$). The black solid boxes indicate unit cells. The green dash boxes in (a) and (b) highlight the local environments around the oxygen octahedra. The orange-colored NbO_6 octahedra in (c) and (d) indicate the octahedra with the same sense of octahedral rotations.

ferroelectricity (HIF) has opened up new avenues for designing polar perovskite-related compounds.[21,22] In HIF, spontaneous polarization is induced by a trilinear coupling term between a polar distortion mode and other two nonpolar oxygen octahedral rotation (OOR) modes in free energy.[21–25]

HIF is commonly found in the layered perovskites without inversion symmetry around the B sites. Ferroelectric properties have been reported for many Ruddlesden–Popper (RP) layered perovskite oxides with a chemical formula of $A'_2(A_{n-1}B_nO_{3n+1})$ such as $Ca_3Ti_2O_7$[26] and $Sr_3M_2O_7$ (M = Zr, Hf, Sn),[27–30] which exhibit OORs represented by $a^-a^-c^+$-type in Glazer notation[31] below Curie temperature, T_C. Yoshida *et al.*[4] have reported for the RP ferroelectrics that T_C linearly increases with a lowering Goldschmidt tolerance factor, τ, defined as follows:[32,33]

$$\tau = \frac{r_A + r_O}{\sqrt{2}(r_B + r_O)} \quad (1)$$

where r_A, r_B, and r_O are the ionic radii of A, B, and O^{2-} ions, respectively. This factor is relevant to the geometric condition of ionic radius for ideal perovskite structures. A value of τ smaller than unity indicates a greater OOR instability and hence enhanced T_C. Fig. 1a shows a schematic of the aristotype RP structure, where the A- and A'-site cations are located in the perovskite slabs and the intervening rocksalt layers, respectively. The BO_6 octahedra are surrounded by four A-site and four A'-site cations, closely resembling the surrounding environments in simple perovskites. This rationalizes the clear correlation between τ and T_C.

HIF has been also demonstrated for Dion–Jacobson (DJ) layered perovskite niobates and tantalates with a general chemical formula of $A'(A_{n-1}B_nO_{3n+1})$. As summarized in Table 1 and shown in Fig. S1 (ESI†), however, the number of reports of HIF DJ phases[34–40] is still limited thus far compared to HIF RP phases. In DJ oxides, A-site and A'-site cations are placed in the perovskite slabs and the intervening layers with CsCl structures, respectively (Fig. 1b). Unlike RP structures, the BO_6 octahedra in DJ phases have significantly different surrounding environments compared to simple perovskites; the A'-site cations are distanced from the octahedra, disrupting the perovskite geometry. Therefore, the influence of A-site and A'-site cations on the structural properties including OOR instability is different from each other.

Table 1 Space group symmetry of the polar phases, octahedral rotation patterns in Glazer notation, and Curie temperatures (T_C) of polar n = 2 Dion–Jacobson double-layered perovskites and their related compounds reported previously

Compound	Space group	Glazer notation	T_C (K)	Ref.
$RbPrNb_2O_7$	$I2cm$	$a^-a^-c^+/-(a^-a^-c^+)$	537[a]	38
$CsSmNb_2O_7$	$P2_1am$	$a^-a^-c^+$	1113	37
$RbSmNb_2O_7$	$I2cm$	$a^-a^-c^+/-(a^-a^-c^+)$	—	37
$CsNdNb_2O_7$	$P2_1am$	$a^-a^-c^+$	625	35
$CsNdTa_2O_7$	$P2_1am$	$a^-a^-c^+$	330	35
$RbNdNb_2O_7$	$I2cm$	$a^-a^-c^+/-(a^-a^-c^+)$	790	35
$RbNdTa_2O_7$	$I2cm$	$a^-a^-c^+/-(a^-a^-c^+)$	500	35
$CsLaNb_2O_7$	$Amm2$	$a^-b^0c^+$	325	39
$CsBiNb_2O_7$	$P2_1am$	$a^-a^-c^+$	1306	36
$RbBiNb_2O_7$	$P2_1am$	$a^-a^-c^+$	1371	36
$RbBiNb_2O_7$	$P2_1am$	$a^-a^-c^+$	1218	40
$LiNdNb_2O_7$[b]	$B2cm$	$a^-a^-c^+/-(a^-a^-c^+)$	—	34
$KNdNb_2O_7$[b]	$Im2m$	$a^0b^+c^0/a^0-b^+c^0$	—	34
$KNdTa_2O_7$[b]	$Im2m$	$a^0b^+c^0/a^0-b^+c^0$	—	34

[a] This compound undergoes a polar-to-polar phase transition at 537 K, below which the number of OOR axes is increased from two to three. In this study, this temperature is regarded as T_C of $RbPrNb_2O_7$ because we focus on the OOR instability. [b] These have intervening layers other than CsCl-type structures.

To extract the effect of the A-site cations on OOR instability, it is beneficial to focus on the DJ phases with identical A'-site and B-site ions but distinct A-site ions. $CsSmNb_2O_7$ has a higher T_C of 1363 K than $CsNdNb_2O_7$ with T_C = 625 K. This is attributed to the smaller ionic radius of Sm^{3+} compared to Nd^{3+}, which results in a smaller value of τ. Moreover, $RbNdNb_2O_7$ (790 K)[35] has higher T_C than $RbPrNb_2O_7$ (537 K),[38] which is ascribed to the smaller ionic radius of Nd^{3+} compared to Pr^{3+}. Thus, the dependence of OOR instability on the ionic radius of A-site ions is explained based on τ. It should be noted that Bi-based DJ oxides $RbBiNb_2O_7$ and $CsBiNb_2O_7$ show much higher T_C's than other DJ oxides, deviating from the trends described above. This is because

the stereochemically active lone pair 6s electrons in Bi^{3+} ions enhance the ferroelectric instability.

The A'-site ions have more complex effects on the crystal structures including the stacking arrangements of perovskite slabs as well as the OOR patterns and instability. DJ phases are stabilized for A' = Cs and Rb, whereas the stacking arrangements become different when A' ions are small alkali ions such as K^+, Na^+, and Li^+, as these ions prefer to lower coordination numbers, disrupting the formation of intervening CsCl-type layers.[34] $CsANb_2O_7$ and $RbANb_2O_7$ (A = Pr, Nd, and Sm) crystallize in polar $P2_1am$ and $I2cm$ structures, adopting different OOR patterns with $a^-a^-c^+$- and $a^-a^-c^+/-(a^-a^-c^+)$-types, respectively, as shown in Fig. 1c and d.[41] (Here, the OOR patterns of the adjacent slabs are written before and behind a slash, and the opposite sense of rotation and tilting is denoted by a prefactor of minus sign.) Rb-based DJ compounds typically exhibit higher T_C values than Cs counterparts for rare-earth DJ phases[35] (see Fig. S1, ESI†). It cannot be hastily concluded that this is due to the smaller ionic radius of Rb^+ ions than that of Cs^+ ions, because they show similar but distinct OOR patterns. Comprehensive understanding of the effects of the A'-site cations on the OOR instability requires systematic variation of the A'-site cations. The structural and dielectric properties have not yet been examined for solid solutions of DJ phases with different OOR patterns thus far.

In this work, we have systematically investigated the relationship between structural and ferroelectric properties of complete solid-solution $Cs_{1-x}Rb_xNdNb_2O_7$ ceramics (x = 0, 0.25, 0.5, 0.75, and 1) with varying Rb/Cs ratio at the A' sites. This system is a rare example of the complete solid solutions with end members exhibiting HIF. To the best of our knowledge, such a complete solid solution has only been reported for $Sr_3(Sn,Zr)_2O_7$.[42] Ferroelectricity was observed for all the samples at both 77 K and room temperature. Variable-temperature synchrotron X-ray diffraction (SXRD) reveals structural phase transitions on cooling from aristotype $P4/mmm$ via intermediate phases to polar $P2_1am$ and $I2cm$ phases for Cs- and Rb-rich compounds, respectively. Their polar-to-nonpolar phase transitions are also tracked by various characterizations including differential scanning calorimetry (DSC), optical second harmonic generation (SHG) measurements, and dielectric permittivity measurements. Noticeably, phase transition temperatures deviate from those predicted based on the Vegard's law. This likely stems from structural frustration effects owing to the disordered arrangement of two types of A'-site alkali metal ions, which determine the sense of OORs between the adjacent slabs.

Experimental

Sample synthesis

Conventional solid-state reaction methods were used to synthesize a series of DJ perovskites $Cs_{1-x}Rb_xNdNb_2O_7$ (x = 0, 0.25, 0.5, 0.75, and 1). The reagent-grade powders of Cs_2CO_3 (99.9%; Kojundo Chemical Laboratory Co. Ltd), Rb_2CO_3 (99.9%; Kojundo Chemical Laboratory Co. Ltd), Nd_2O_3 (99.9%; Kojundo Chemical Laboratory Co. Ltd), and Nb_2O_5 (99.9%; Sigma-Aldrich Co. Ltd) were chosen as raw materials. The raw materials were weighted to ensure a 20% excess of alkali metal elements relative to the stoichiometric compositions, followed by thorough mixing using an agate mortar. Following grinding with ethanol for 15 min, the mixtures were transferred to an 80 °C oven for drying before being compacted into 20 mm diameter pellets at 40 MPa. These pellets were then placed on Pt sheets in alumina crucibles, subject to calcination at 850 °C for 24 h, and subsequently ground into powders. A double-step pressing process was performed; the ground powders were initially pelletized at 40 MPa using a uniaxial pressing, followed by pressing the pellets to a hydrostatic 200 MPa pressure for 15 min. The resultant pellets were sintered at 1000 °C for 48 hours, yielding dense pellets displaying a light violet coloration due to the 4f–4f transition in Nd ions. The relative densities of sintered pellets were *ca.* 95% for all the compositions.

Surface morphology characterization and chemical element analysis

The scanning electron microscopy (SEM) equipped with energy dispersive X-ray spectroscopy (EDS) was used to observe the microstructures and measure chemical compositions of $Cs_{1-x}Rb_xNdNb_2O_7$ (x = 0, 0.25, 0.5, 0.75, and 1) ceramics, respectively, with a JCM-7000 instrument (JEOL Ltd.). The applied voltage was set as 15.0 keV.

SXRD

Variable-temperature synchrotron SXRD patterns were measured with MYTHEN solid-state detectors installed at SPring-8 BL02B2 beamline equipping a Debye–Scherrer camera *via* two types of measurement modes referred to as single- and double-step modes described in ref. 43 in detail. In the single-step modes, XRD patterns were recorded for an exposure time of 14 s by sweeping temperature from 1100 to 300 K at a rate of 20 K min^{-1}, resulting in a temperature resolution of *ca.* 5 K. In the double-step mode, XRD patterns were collected at various temperatures for an exposure time of 180 s by increasing temperature from 300 to 1100 K with intervals of 50 or 100 K in a stepwise way to obtain diffraction data suitable for Rietveld refinements. Silica or Lindemann glass capillary tubes with 0.1 mm diameter were used to load ground powder samples. To reduce the negative effects of the preferred orientation, the capillary tubes were always rotated during measurements. The monochromated X-ray beam has λ = 0.67049 or 0.669077 Å to avoid Nb K-edge absorption (0.6532 Å) and detect the lowest angle peaks within 2θ range of the beamline ($\geq 2^\circ$). The FullProf Suite was used to perform Rietveld refinements against SXRD patterns recorded using the double-step measurement mode.[44] The VESTA code[45] was employed to visualize crystal structures and calculate bond valence sums (BVSs) with the bond valence parameters reported in ref. 46 to verify the validity of the refined structure.

Raman spectra measurement

A micro-Raman spectrometer equipped with a 532 nm semiconductor laser (XploRA, HORIBA, Ltd) was used to record the Raman spectra of samples from 50 to 1050 cm^{-1}.

DSC

DSC was measured using Rigaku Thermo plus DSC8270. The data from RT to 1273 K were collected at a heating and cooling rate of 10 K min^{-1}.

Temperature-dependent SHG measurement

Optical SHG signals were measured in reflection geometry with an 800-nm fundamental beam (Ti:sapphire laser, 80 fs pulses, 1 kHz repetition rate). Temperature control was achieved using a home-built heater.

Temperature-dependent permittivity measurement

For the temperature-dependent permittivity measurement, the sintered pellets were shaped to thin discs with a thickness of 0.3–0.5 mm followed by putting Pt films on both sides by sputtering. An LCR meter (IM3536, HIOKI Co. Ltd.) connected to a cryostat (TERADA Co. Ltd.) and a temperature controlling stage (Linkam Scientific Instruments Ltd, 19624L) were used to measure capacitances and dielectric losses in low- (5–300 K) and high-temperature (300–873 K) regions, respectively.

Electric polarization-field curve measurement

Electric polarization-field (*P–E*) curves for all the compositions were measured with a Radiant Precision LCII ferroelectric tester and a Trek 609B voltage amplifier at 77 K and RT to characterize the ferroelectric properties. The samples were polished so that they had a thickness of 0.1–0.2 mm. The sample pellets with Pt electrodes were put into liquid nitrogen to record low-temperature data. For RT measurements, the pellet samples were immersed in silicon oil to avoid the electric leakage in air. Gold film electrodes were deposited on the pellets because they were not dispersed into silicon oil. Remanent hysteresis measurement methods implemented in the ferroelectric tester were employed to exclude the effects of leaky current and linear response. The maximum amplitude of electric field was 100 kV cm^{-1}. The *P–E* curves were obtained from three pellet samples for each composition to consider statistical errors and thereby guarantee the data reliability.

Results

Room-temperature structures of $Cs_{1-x}Rb_xNdNb_2O_7$

The room-temperature phases of $Cs_{1-x}Rb_xNdNb_2O_7$ are identified in this section. Fig. 2a shows the room-temperature SXRD patterns of $Cs_{1-x}Rb_xNdNb_2O_7$. The SXRD patterns of $CsNdNb_2O_7$ and $RbNdNb_2O_7$ are in good agreement with those reported previously.[35,47] Zhu *et al*. studied the crystal structures for the end members by a combination of X-ray and neutron diffractions in detail.[35] $CsNdNb_2O_7$ and $RbNdNb_2O_7$ crystalize in the polar structures with $P2_1am$ (Fig. 1c) and $I2cm$ (Fig. 1d) space group symmetry, the OOR patterns of which are denoted by $a^-a^-c^+/a^-a^-c^+$ and $a^-a^-c^+/-(a^-a^-c^+)$, respectively. In $CsNdNb_2O_7$, the adjacent AB_2O_7 double perovskite slabs with $a^-a^-c^+$-type OORs are stacked in a primitive manner. Meanwhile, each perovskite slab of $RbNdNb_2O_7$ shows $a^-a^-c^+$-type OORs with the sense of OORs being opposite to that in the adjacent slabs, as depicted in Fig. 1d. This results in a body-centered *I*-lattice, making the conventional unit cell doubled compared to that of $CsNdNb_2O_7$. The OOR modes for the $P2_1am$ and $I2cm$ structures transform like the direct sums of irreducible representations (irreps) of $P4/mmm$, $M_2^+ \oplus M_5^-$ and $A_2^+ \oplus A_5^-$, respectively. These direct sums induce common polar distortion modes transforming like irrep Γ_5^-. Zhu *et al.* suggested that the distinct stacking of adjacent layers is attributed to the bonding preference of *A*- and *A*′-site cations and the minimization of O–O repulsion.[35]

The overall features of SXRD patterns are common to the $Cs_{1-x}Rb_xNdNb_2O_7$ solid solutions, indicating that DJ structures are maintained in the whole compositional range. This is also corroborated by the similar Raman spectra of the solid solutions (see Fig. S2, ESI†). The EDS analysis reveals that the *A*′-site Rb/Cs ratio is comparable to nominal Rb/Cs ratio as shown in Fig. S3 (ESI†). These results suggest that the $CsNdNb_2O_7$–$RbNdNb_2O_7$ system shows complete miscibility, even when the ionic radius of Cs^+ is 15% larger than that of Rb^+. The lowest-angle diffraction peaks relevant to the out-of-plane lattice constants monotonously shift to the higher-angle side with increasing Rb contents, as shown in Fig. 2b, indicating that larger Cs ions are successfully replaced with smaller Rb ions. This is likely because of the structural flexibility of the intervening layers accommodating the *A*′-site cations.

The distinct features of the SXRD patterns that distinguish the $P2_1am$ and $I2cm$ structures are required to find the compositional phase boundary. The reflection conditions for $P2_1am$ are $h00$ and $h0l$: $h = 2n$ with n being integer, while those for $I2cm$ are hkl: $h + k + l = 2n$ and $h0l$: $l = 2n$. According to the reflection rules, the space group symmetry of Cs-rich compositions, $Cs_{1-x}Rb_xNdNb_2O_7$ with $x = 0$ and 0.25, is identified as $P2_1am$, while that of Rb-rich compositions, $x = 0.5$, 0.75 and 1, is determined to be $I2cm$. Fig. 2c displays the selected angle region including 121 and 123 diffraction peaks for the $P2_1am$ and $I2cm$ structures, respectively, as typical features distinguishing the two phases. The $P2_1am$ phases exhibit 121 diffraction peaks around $2\theta = 16.2^\circ$, whereas the $I2cm$ phases show no peaks in this region. Meanwhile, the $I2cm$ phases exhibit 123 diffraction peaks around $2\theta = 16.7^\circ$, whereas the $P2_1am$ phases show no peaks in this angle range. The $I2cm$ phases undergo cell doubling along the c axis with respect to the $P2_1am$ phase. Therefore, the 121 diffraction peak for the $P2_1am$ phases corresponds to the 122 diffraction peak for the $I2cm$ phase, which is prohibited for the body-centered lattice; $h + k + l$ is odd. Meanwhile, the 123 diffraction for the $I2cm$ phase corresponds to the half-integer $12\frac{3}{2}$ diffraction for the $P2_1am$ phase, resulting in the absence of the peaks. Thus, the two phases can be readily distinguished by examining the 121 diffraction for the $P2_1am$ phases and the 123 diffraction for the $I2cm$ phases. Fig. 2d presents profile fitting of the SXRD pattern for $Cs_{0.5}Rb_{0.5}NdNb_2O_7$ with a $I2cm$ structural model as a representative Rietveld refinement result. Acceptable fitting was obtained for all the room-temperature SXRD patterns with the

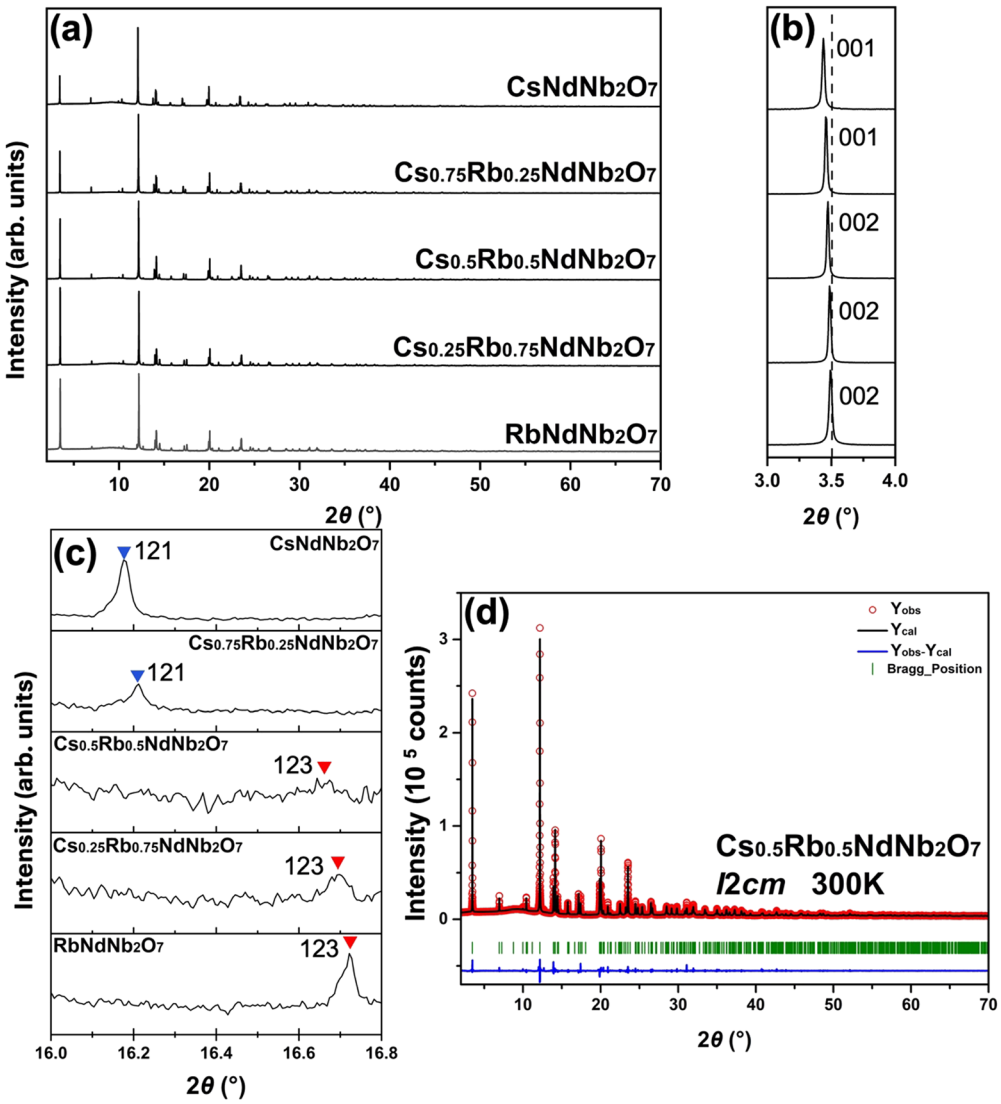

Fig. 2 Phase identification for $Cs_{1-x}Rb_xNdNb_2O_7$ (x = 0, 0.25, 0.5, 0.75, and 1) at room temperature. Panel (a) depicts the whole SXRD patterns. Panel (b) highlights the lowest-angle 001 or 002 diffraction peaks for the $P2_1am$ and $I2cm$ phases, respectively. Panel (c) shows the selected diffraction peaks that distinguish the $P2_1am$ and $I2cm$ phases. (d) Rietveld refinement result for the room-temperature SXRD pattern of $Rb_{0.5}Rb_{0.5}NdNb_2O_7$ with an $I2cm$ structural model.

structural models identified above. The close inspection of the XRD patterns revealed that all the samples contain negligible secondary phases, verifying the good quality of the samples.

Phase transition pathways of $Cs_{1-x}Rb_xNdNb_2O_7$

To construct a temperature-composition phase diagram in the $Cs_{1-x}Rb_xNdNb_2O_7$ system, variable-temperature SXRD measurements were conducted with a fine temperature resolution of *ca.* 5 K using the single-step measurement mode. The wavelength used in the measurements for $CsNdNb_2O_7$ and $RbNdNb_2O_7$ is 0.669077 Å, while that for $Cs_{0.75}Rb_{0.25}Nb_2O_7$, $Cs_{0.5}Rb_{0.5}Nb_2O_7$ and $Cs_{0.25}Rb_{0.75}Nb_2O_7$ is 0.670489 Å. Fig. 3 shows the selected angle region of temperature-dependent SXRD patterns for $Cs_{1-x}Rb_xNdNb_2O_7$. The phase transition behavior of the end members $CsNdNb_2O_7$ and $RbNdNb_2O_7$ is almost consistent with that reported by Zhu *et al.*, albeit with a minor discrepancy.[35] $CsNdNb_2O_7$ goes through a polar-to-nonpolar phase transition from the $P2_1am$ phase with $a^-a^-c^+$-type OORs to a monoclinic $C2/m$ phase with $a^-b^0c^-$-type OORs at 630 K, and then transforms to the aristotype $P4/mmm$ phase at 790 K on heating (see Fig. 3a), in good agreement with the report by Zhu *et al.*[35] Meanwhile, upon heating, $RbNdNb_2O_7$ undergoes a polar-to-nonpolar phase transition from the $I2cm$ phase with $a^-a^-c^+/-(a^-a^-c^+)$-type OORs to a $Cmca$ phase with $a^-b^0c^-/-(a^-b^0)c^-$-type OORs at 740 K, and then transforms to an undistorted $P4/mmm$ phase at 880 K (see Fig. 3e). The previous neutron powder diffraction study revealed a phase transition from the $Cmca$ phase to an $I4/mcm$ phase with $a^0a^0c^-/a^0a^0-c^-$-type OORs at 865 K on heating.[35] This was not detected by our SXRD likely due to the poor sensitivity of X-ray to the positions of light atoms. The $I4/mcm$ phase exhibits the OORs, whereas the $P4/mmm$ phase does not; the difference

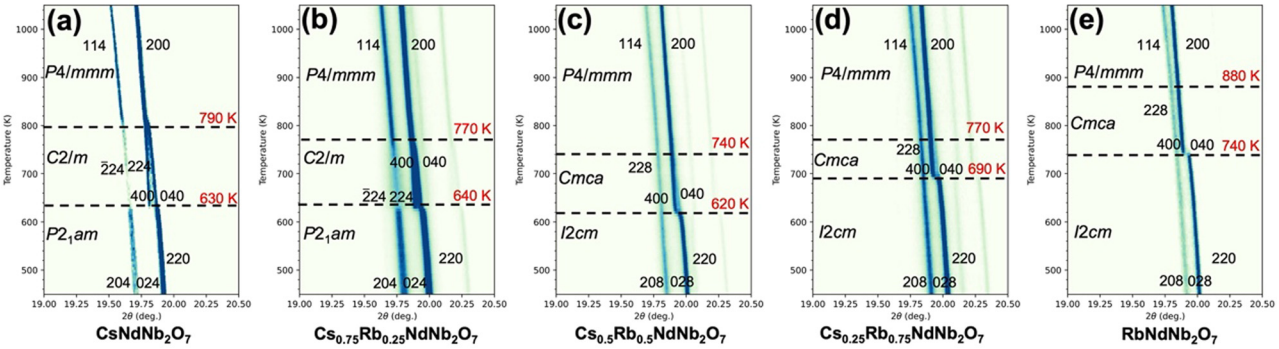

Fig. 3 Two-dimensional plots of the temperature-dependent SXRD patterns around $2\theta = 20^\circ$ for $Cs_{1-x}Rb_xNdNb_2O_7$ with x = (a) 0, (b) 0.25, (c) 0.5, (d) 0.75, and (e) 1.

between the *I*4/*mcm* and *P*4/*mmm* phases lies not in the cation's positions but in the oxygen's positions. The resultant superlattice reflections of the *I*4/*mcm* phase are too weak to be detected by X-ray. In both the end members, the number of OOR axes increases as the phase transitions occur upon cooling, indicating that the phase transitions are mainly driven by the OOR instability. The phase transition behavior of the solid solutions is categorized into two distinct groups; the Cs-rich $Cs_{0.75}Rb_{0.25}NdNb_2O_7$ sample follows the same phase transition pathway as $CsNdNb_2O_7$ (*P*2$_1$*am*–*C*2/*m*–*P*4/*mmm*) (see Fig. 3b), while the Rb-rich $Cs_{0.5}Rb_{0.5}NdNb_2O_7$ and $Cs_{0.25}Rb_{0.75}NdNb_2O_7$ samples follow the same phase transition pathway as $RbNdNb_2O_7$ (*I*2*cm*–*Cmca*–(*I*4/*mcm*–)*P*4/*mmm*) (see Fig. 3c and d).

Let us see the variation of diffraction patterns with temperature in detail. Fig. 3a and b depict the variable-temperature SXRD patterns around $2\theta = 20^\circ$ for the Cs-rich $CsNdNb_2O_7$ and $Cs_{0.75}Rb_{0.25}NdNb_2O_7$ samples, respectively. Upon heating, a single 220 diffraction peak of the polar *P*2$_1$*am* phase splits into 400 and 040 diffraction peaks of the nonpolar *C*2/*m* phase. Meanwhile, 204 and 024 diffraction peaks of *P*2$_1$*am* phase are converted to 224 and $22\bar{4}$ diffraction peaks of the *C*2/*m* phase. These observations reflect the unit-cell doubling from an orthorhombic $\sqrt{2}a_0 \times \sqrt{2}a_0 \times c_0$ cell to a monoclinic $2a_0 \times 2a_0 \times 2c_0$ cell, where a_0 and c_0 are the lattice constants of the aristotype *P*4/*mmm* phase. As shown in Fig. S4a and b (ESI†), this phase transition is also reflected by 200 and 020 diffraction peaks of the *P*2$_1$*am* phase around $2\theta = 14^\circ$ merging into a single 220 peak of the *C*2/*m* phase. The *P*2$_1$*am*-to-*C*2/*m* phase transition is a ferroelectric-to-paraelectric phase transition, as confirmed by optical SHG, permittivity, and *P*–*E* curve measurements below. The Curie temperatures (T_C) are 630 and 640 K for $CsNdNb_2O_7$ and $Cs_{0.75}Rb_{0.25}NdNb_2O_7$, respectively. Another phase transition was observed at higher temperatures from 400 and 040 diffraction peaks of the nonpolar *C*2/*m* phase merging into a single 200 diffraction peak of the *P*4/*mmm* phase due to the unit-cell reduction from $2a_0 \times 2a_0 \times c_0$ for the *C*2/*m* phase to $a_0 \times a_0 \times c_0$ for the *P*4/*mmm* phase. This phase transition is also reflected by $\bar{2}24$ and 224 diffraction peaks of the *C*2/*m* phase around $2\theta = 20^\circ$ merging into a single 114 diffraction peak of the *P*4/*mmm* phase [see also Fig. S4c and d, ESI†]. The *C*2/*m*-to-*P*4/*mmm* phase transition temperatures are 790 and 770 K for $CsNdNb_2O_7$ and $Cs_{0.75}Rb_{0.25}NdNb_2O_7$, respectively.

Fig. 3c–e depict the variable-temperature SXRD patterns around $2\theta = 20^\circ$ for the Rb-rich samples. Upon heating, a single 220 diffraction peak of the polar *I*2*cm* phase splits into 400 and 040 diffraction peaks of the nonpolar *Cmca* phases due to the unit-cell doubling from $\sqrt{2}a_0 \times \sqrt{2}a_0 \times 2c_0$ for *I*2*cm* to $2a_0 \times 2a_0 \times c_0$ for *Cmca* [see also Fig. S5a–c, ESI†]. These phase transitions are ferroelectric–paraelectric transitions. The T_C values are 620, 690, and 740 K for $Cs_{1-x}Rb_xNdNb_2O_7$ with x = 0.5, 0.75, and 1, respectively. The phase transitions from the *Cmca* to *P*4/*mmm* phases accompany subtle changes in the SXRD patterns. As seen in Fig. S5d–f (ESI†), the 400 and 040 diffraction peaks of the *Cmca* phase merge into a single 200 peak reflection of the *P*4/*mmm* phase due to the cell-size reduction from $2a_0 \times 2a_0 \times 2c_0$ to $a_0 \times a_0 \times c_0$. The phase transition temperatures are determined as 740, 770, and 880 K for $Cs_{1-x}Rb_xNdNb_2O_7$ with x = 0.5, 0.75, and 1, respectively. As mentioned above, it should be noted that our SXRD studies may overlook the existence of the *I*4/*mcm* phase due to the poor sensitivity of XRD to oxygen's positions.

Structural refinements by Rietveld methods

We identified the room-temperature and high-temperature phases for all the compositions based on the SXRD data measured using the single-step measurement mode above. Rietveld refinements were performed for the variable-temperature SXRD data collected with the double-step measurement mode to verify our phase identification and to extract structural parameters. Fig. S6–S10 (ESI†) depict the results of Rietveld refinements for variable-temperature SXRD patterns. The refined structural parameters for the representative data are summarized in Tables S1–S15 (ESI†). The refined Rb/Cs ratios at the A' sites for the RT SXRD patterns are highly close to the nominal Rb/Cs ratios, as shown in Fig. S3 (ESI†). Therefore, the Rb/Cs ratios were fixed to the nominal values. The resultant fits gave small reliability factors for all the data. As shown in Table S16 (ESI†), the cation BVSs calculated for all the refined structures are consistent with their formal charges, corroborating the validity of the structural models. Note that two-phase models were used for the SXRD patterns of $RbNdNb_2O_7$ at 750 K (*I*2*cm*: 71.39%;

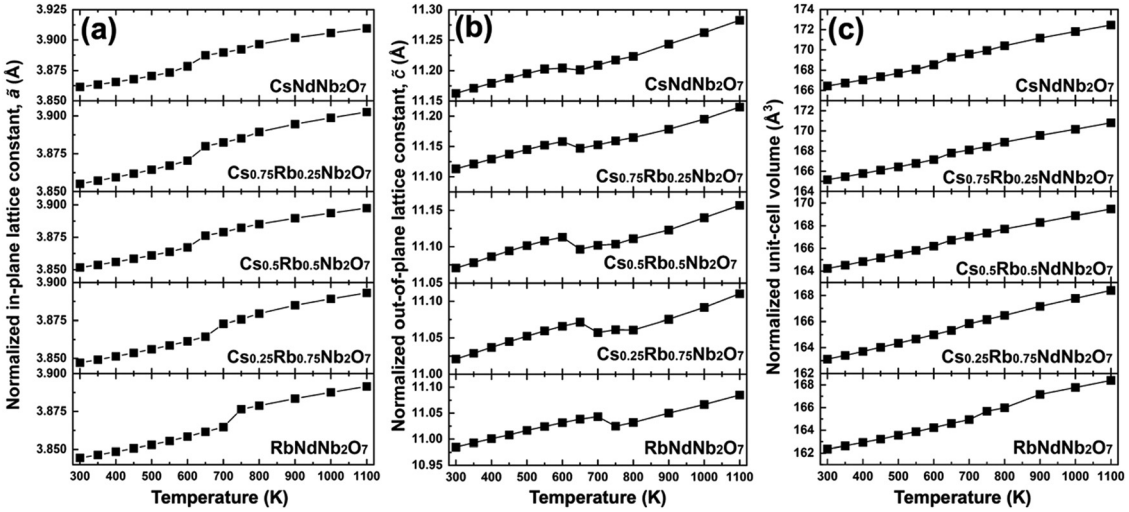

Fig. 4 Normalized in-plane and out-of-plane lattice constants, (a) $\tilde{a}$ and (b) $\tilde{c}$, respectively, and (c) normalized unit-cell volume as a function of temperature for all the solid solutions $Cs_{1-x}Rb_xNdNb_2O_7$ with x = 0, 0.25, 0.5, 0.75, and 1.

Cmca: 28.61%) and $Cs_{0.75}Rb_{0.25}NdNb_2O_7$ at 650 K ($P2_1am$: 8.91%; $C2/m$: 91.09%). Based on the refined structures, the cation polar displacements in each phase will be discussed later.

Temperature dependence of lattice constants

The variation of lattice constants with temperature is studied to examine the phase transition behavior. The normalized in-plane lattice constants are defined as $\tilde{a} = \sqrt{ab/2}$ for the $I2cm$ and $P2_1am$ phases, which have $\sqrt{2}a_0 \times \sqrt{2}a_0 \times 2c_0$ and $\sqrt{2}a_0 \times \sqrt{2}a_0 \times c_0$ unit cells, respectively; $\tilde{a} = \sqrt{ab/4}$ for the $C2/m$ and *Cmca* phases, possessing $2a_0 \times 2a_0 \times c_0$ and $2a_0 \times 2a_0 \times 2c_0$ unit cells, respectively; and $\tilde{a} = a$ for the $P4/mmm$ phase. The normalized out-of-plane lattice constants are defined as $\tilde{c} = c$ for the $P2_1am$ and $P4/mmm$ phases, $\tilde{c} = c\sin\beta$ for the $C2/m$ phase, and $\tilde{c} = c/2$ for the $I2cm$ and *Cmca* phases. The normalized in-plane and out-of-plane lattice constants, $\tilde{a}$ and $\tilde{c}$, were plotted as a function of temperature in Fig. 4a and b. Both the in-plane and out-of-plane lattice constants exhibit an increase with increasing averaged radius of the A'-site cations, leading to an increase in the normalized cell volume defined as $\tilde{V} = \tilde{a}^2\tilde{c}$, as shown in Fig. 4c. It is obvious that the lattice constants of each phase increase upon heating for all the compositions overall due to thermal expansion. To observe phase transitions more clearly, changes in volume over changes in temperature, $\frac{\Delta\tilde{V}}{\Delta T}$, were plotted as a function of temperature in Fig. S11 (ESI†). The $\frac{\Delta\tilde{V}}{\Delta T}$ values exhibit anomalies at the phase transition temperatures. Such discrete changes in the lattice constants indicate first-order phase transitions. The $\frac{\Delta\tilde{V}}{\Delta T}$ anomalies are more obvious for the polar-to-nonpolar phase transitions than for the nonpolar-to-nonpolar phase transitions, indicating that the unit-cell expansion is significant for polar-to-nonpolar phase transitions.

Phase transitions detected by DSC

DSC measurements were conducted on both heating and cooling processes to observe the thermal behavior across phase transitions including reversibility and hysteresis. Fig. 5a depicts the DSC curves for all the compositions and Fig. S12 (ESI†) shows the details around peaks. Endothermic and exothermic peaks are observed upon heating and cooling, respectively, around the polar-to-nonpolar $I2cm$-to-*Cmca* or $P2_1am$-to-$C2/m$ phase transition temperatures, indicating the reversibility of the phase transitions. The averaged values of endothermic and exothermic peak temperatures are summarized in Table S17 (ESI†) for $Cs_{1-x}Rb_xNdNb_2O_7$ with x = 0, 0.25, 0.5, 0.75, and 1, which are close to the polar-to-nonpolar phase transition temperatures obtained by the SXRD data. The endothermic peak temperatures upon heating are higher than the exothermic peak temperatures upon cooling. The thermal hysteresis behavior indicates that the polar-to-nonpolar phase transitions are first-order. Meanwhile, no obvious peaks are observed for other nonpolar-to-nonpolar phase transitions. The large latent heats for the polar-to-nonpolar phase transitions are reflected by the sharp changes in lattice constants for the polar-to-nonpolar phase transitions, as observed in Fig. S11 (ESI†). The smooth changes in lattice constants across the nonpolar-to-nonpolar phase transitions reflect small latent heats, hampering the peaks in the DSC curves.

Noncentrosymmetry probed by optical SHG

Optical SHG is one of the most useful probes of noncentrosymmetry.[1,2] Variable-temperature SHG measurements were performed to confirm the polar-to-nonpolar $I2cm$-to-*Cmca* and $P2_1am$-to-$C2/m$ phase transitions for Rb-rich and Cs-rich pellet samples, respectively. Fig. 5b depicts the temperature-dependent optical SHG signals for all the compositions. Finite SHG signals at room temperature agree with the SXRD results showing that all the samples adopt polar structures. The SHG signals become lower upon heating, and steeply go down to

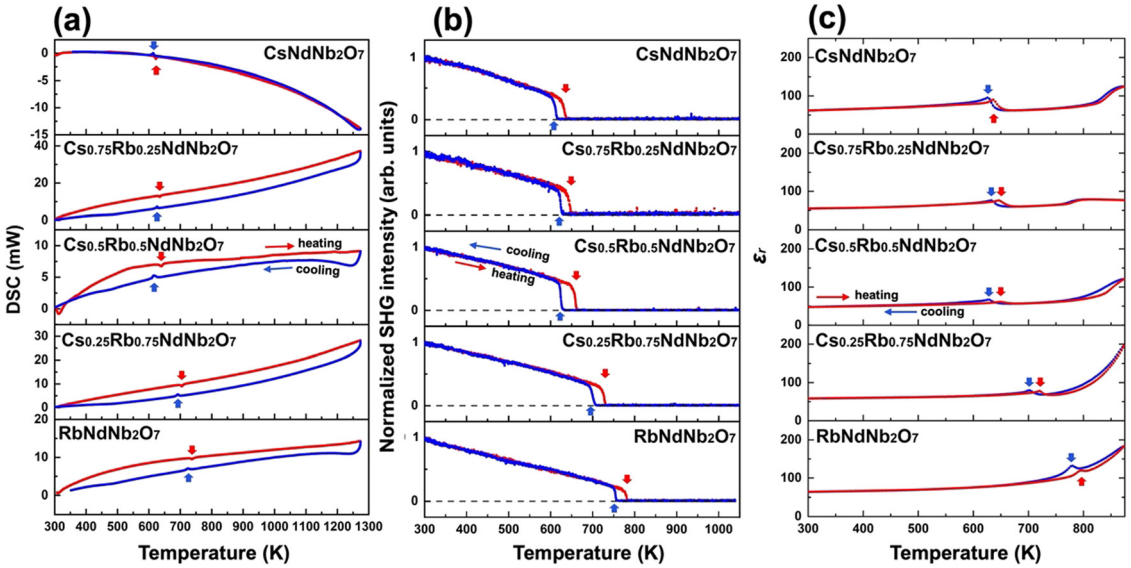

Fig. 5 Multiple variable-temperature measurements for detecting phase transitions. (a) DSC and (b) SHG signals and (c) permittivity as a function of temperature for $Cs_{1-x}Rb_xNdNb_2O_7$ with x = 0, 0.25, 0.5, 0.75, and 1. The red and blue arrows indicate the polar-to-nonpolar phase transition temperatures during the heating and cooling processes, respectively.

negligible values near the polar-to-nonpolar phase transition temperatures, corroborating the emergence of inversion symmetry. The thermal hysteresis between heating and cooling curves reveals the first-order phase transitions for this system, consistent with the DSC analysis. The polar-to-nonpolar phase transition temperatures detected by SHG are summarized in Table S17 (ESI†). These temperatures are also consistent with those determined by SXRD and DSC.

Temperature dependence of permittivity

Other common methods to reveal polar-to-nonpolar phase transitions include variable-temperature permittivity measurements. Fig. 5c plots the permittivity for all the compositions as a function of temperature. The permittivity curves show cusps at the polar-to-nonpolar phase transition temperatures for all the samples, and Fig. S13 (ESI†) shows detailed peak positions. The polar-to-nonpolar phase transition temperatures are summarized in Table S17 (ESI†). The observed thermal hysteresis is consistent with the DSC and SHG results. The Cs-rich $CsNdNb_2O_7$ and $Cs_{0.75}Rb_{0.25}NdNb_2O_7$ samples exhibit a steep rise in the permittivity near the phase transition temperatures between the *C*2/*m* and *P*4/*mmm* phases, accompanied by an increase in dielectric loss (see Fig. S14a and b, ESI†), whereas such a sudden rise is not observed for the Rb-rich samples (see Fig. S14c–e, ESI†). Fig. S15 (ESI†) presents the low-temperature permittivity and dielectric loss. The absence of anomaly at low temperatures indicates that the room-temperature phases persist down to 5 K.

Microstructure of the ceramic samples and demonstration of ferroelectricity

A plan-view SEM image for a $Cs_{0.5}Rb_{0.5}NdNb_2O_7$ ceramic pellet depicted in Fig. 6a reveals a dense packing of plate-like crystalline particles, consistent with a high relative density of 95%. Sintered ceramic samples with other compositions also exhibit a dense particle packing as shown in Fig. S16 (ESI†). *P*–*E* curves were recorded for the pellet samples at 77 K and room temperature to reveal the ferroelectric properties. Fig. 6b depicts the *P*–*E* curves for $Cs_{0.5}Rb_{0.5}NdNb_2O_7$ measured at room temperature with various electric-field amplitudes, as representative data. The observed hysteresis curves demonstrate ferroelectricity at room temperature. Fig. 6c shows the remanent *P*–*E* curves measured at room temperature. The remanent polarization is 0.7 μC cm^{-2} with an electric-field amplitude of 100 kV cm^{-1} at room temperature. As shown in Fig. S17 (ESI†), the hysteretic behavior of remanent *P*–*E* curves was observed at room temperature for all the compositions, demonstrating their room-temperature ferroelectricity. The room-temperature remanent polarization values increase with increasing Rb concentrations, as shown in Fig. 6d. This tendency was observed for DJ $CsSmNb_2O_7$ and $RbSmNb_2O_7$, the room-temperature polarization values of which are 2.0 μC cm^{-2} at 70 kV cm^{-1} and 5.3 μC cm^{-2} at 60 kV cm^{-1}, respectively.[37] Fig. S18a and b (ESI†) depict the coercive fields at 77 K and room temperature as a function of the Rb concentrations. The coercive fields do not strongly depend on temperature. The hysteresis loops observed at 77 K for all the solid solutions shown in Fig. S17 (ESI†) reveal that the polar $P2_1am$ or *I*2*cm* structures are kept at low temperatures, in good agreement with the low-temperature permittivity curves.

Discussion

Compositional variation of polar distortions

Here, let us discuss the compositional variation of polar distortions in $Cs_{1-x}Rb_xNdNb_2O_7$. The *I*2*cm* and $P2_1am$ symmetries

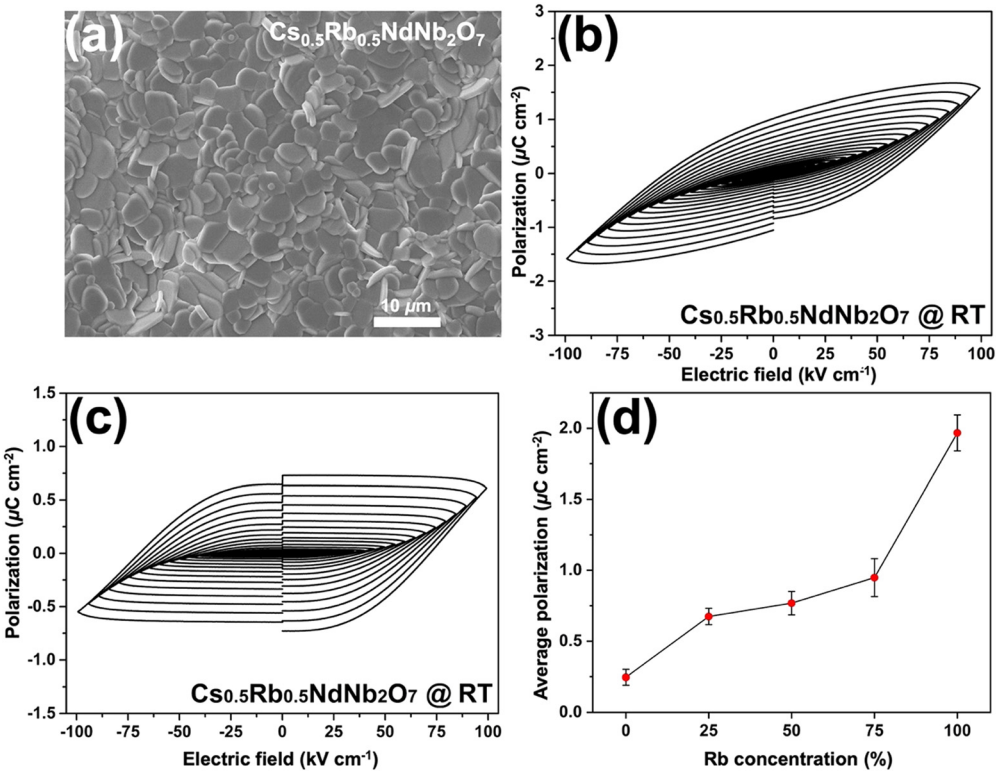

Fig. 6 Microstructure observation and ferroelectric switching experiments. (a) Plan-view scanning electron microscope (SEM) image for the $Cs_{0.5}Rb_{0.5}Nb_2O_7$ ceramic pellet. (b) Polarization-electric field (P–E) curve and (c) remanent P–E curve for $Cs_{0.5}Rb_{0.5}Nb_2O_7$. (d) Averaged remanent polarization for $Cs_{1-x}Rb_xNdNb_2O_7$ (x = 0, 0.25, 0.5, 0.75, and 1).

are established by a direct sum of irreps $A_2^+ \oplus A_5^-$ and $M_2^+ \oplus M_5^-$, respectively. Here, the M_2^+ and M_5^- distortion modes in the $P2_1am$ structure correspond to an $a^0a^0c^+$-type of rotation and an $a^-a^-c^0$-type of tilting, respectively. The combination of these OORs induces a polar distortion mode transforming like irrep Γ_5^- through a trilinear coupling term in the free energy $F_{tri} \propto \eta(M_2^+)\eta(M_5^-)\eta(\Gamma_5^-)$, that is, a HIF mechanism. Meanwhile, the A_2^+ and A_5^- modes in the $I2cm$ structure correspond to an $a^0a^0c^+/a^0a^0{-}c^+$-type of rotation and an $a^-a^-c^0/{-}(a^-a^-)c^0$-type of tilting, respectively. The coupling of these OORs yields the Γ_5^- polar mode due to a similar trilinear coupling to that in the $P2_1am$ structure.

Here, the polar distortions are analyzed by decomposing the polar displacements into the contributions from each cation. The polar displacements of cations are defined as the relative positions of cations with respect to the mass centers of coordination oxygen polyhedra projected into the polar a axis, where $A'O_8$ cuboids, NdO_{12} dodecahedra, and NbO_6 octahedra are regarded as the coordination oxygen polyhedra. Fig. 7 depicts the polar displacements of each cation. Overall, the displacements of high-valent A-site Nd^{3+} and B-site Nb^{5+} ions are larger than those of monovalent A'-site Cs^+/Rb^+ ions. This indicates that the contributions of A-site and B-site cations to polarization are larger than those of A'-site ions, in good agreement with the previous first-principles calculations for $Pmc2_1$ $CsLaNb_2O_7$.[48] The displacements of Nd and A'-site ions show a maximum for $Cs_{0.5}Rb_{0.5}LaNb_2O_7$, while that of Nb ions

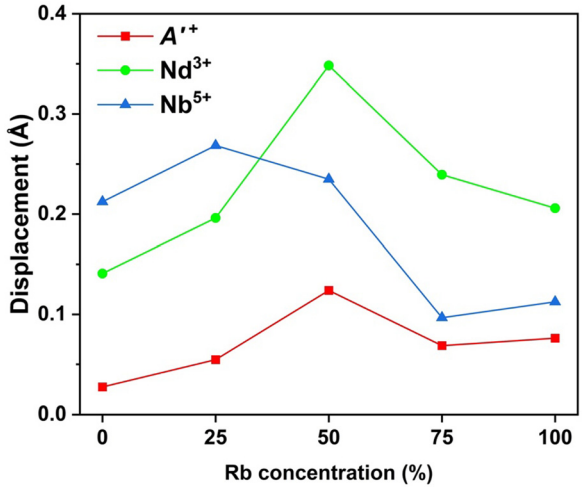

Fig. 7 Polar cation displacements defined as the relative positions of cations with respect to the mass centers of coordination anion polyhedra projected into the polar a axis in $Cs_{1-x}Rb_xNdNb_2O_7$ (x = 0, 0.25, 0.5, 0.75, and 1).

becomes the largest for $Cs_{0.75}Rb_{0.25}LaNb_2O_7$. These results appear to be in contrast with the behavior of remanent polarization, which monotonously increases with increasing Rb content (see Fig. 6d). The discrepancy partly stems from the fact that the measured polarizations were still not saturated at our maximum electric fields. In addition, the particle size and

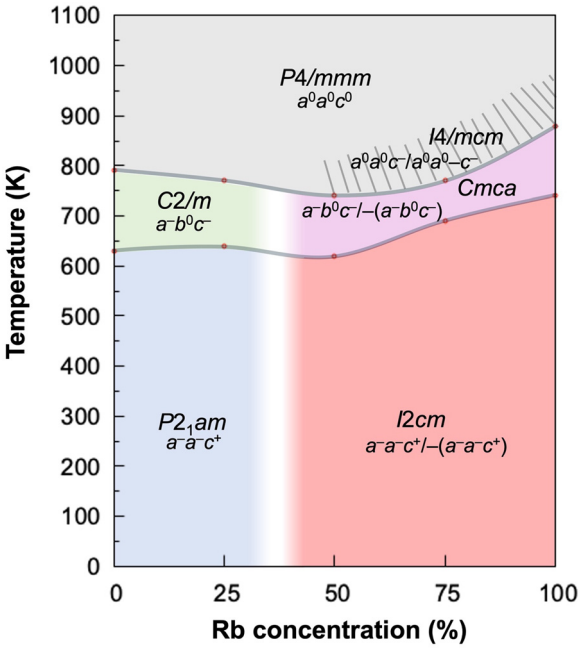

Fig. 8 Temperature-composition phase diagram of the $Cs_{1-x}Rb_xNdNb_2O_7$ system.

shape depend on the Rb contents as shown in the SEM images (see Fig. S16, ESI†). Such microstructure difference can influence the magnitude of polarization, resulting in the absence of correlation between crystal structures and measured polarization values.

Temperature-composition phase diagram

In the last part of this paper, let us discuss the influence of A'-site ions on the phase stability and phase transition temperatures. Fig. 8 illustrates the phase diagram of the $Cs_{1-x}Rb_xNdNb_2O_7$ system constructed based on the SXRD, DSC, optical SHG, and permittivity results. The shaded area indicates the region where the tetragonal *I*4/*mcm* phase was previously reported, although it has not been detected by our SXRD study probably due to the poor sensitivity of oxygen positions. The phase boundary between the $P2_1am$ and *I*2*cm* (*C*2/*m* and *Cmca*) phases falls within the range from 25 to 50 mol% of Rb concentration, as represented by the light-colored area.

As for the Cs-rich group including $CsNdNb_2O_7$ and $Cs_{0.75}Rb_{0.25}NdNb_2O_7$, the nonpolar-to-nonpolar (*C*2/*m*-to-*P*4/*mmm*) phase transition temperatures become lower with increasing Rb concentrations, whereas the polar-to-nonpolar ($P2_1am$-to-*C*2/*m*) ferroelectric transition temperatures are slightly enhanced with higher Rb concentrations. As for the Rb-rich group including $Cs_{1-x}Rb_xNdNb_2O_7$ with x = 0.5, 0.75, and 1, both the nonpolar-to-nonpolar *Cmca*-to-*P*4/*mmm* and polar-to-nonpolar *I*2*cm*-to-*Cmca* phase transition temperatures become higher with increasing Rb concentrations. In both the groups, the polar-to-nonpolar phase transitions are accompanied by a change in the number of OOR axes from three to two, while the nonpolar-to-nonpolar phase transitions involve a reduction of the number of OOR axes from two to zero. It is commonly understood that the OOR instability increases with decreasing *A*-site cation's radii in perovskite-related compounds, letting us infer that both the polar-to-nonpolar and nonpolar-to-nonpolar phase transition temperatures monotonously increase with increasing Rb concentrations. However, the two phase-transition temperatures of the solid solutions do not show a monotonous increase with an increase in the Rb concentration across a whole compositional range, largely deviating from Vegard's law with non-negligible downward bowing. This is most likely because the random arrangement of the A'-site Cs and Rb ions leads to structural frustration effects on the emergence of OORs. The Cs ions prefer the same sense of OORs ($a^-a^-c^+/a^-a^-c^+$) in the adjacent double-perovskite layers, whereas the Rb ions favor the opposite sense of OORs ($a^-a^-c^+/-(a^-a^-c^+)$); the stable OOR patterns cannot be readily determined when the Cs and Rb ions are randomly placed at the A' sites, suppressing the phase transitions. This behavior is reminiscent of the suppression of magnetic phase transition in magnetically frustrated systems, which involve the coexistence of ferromagnetic and antiferromagnetic interactions or the geometric magnetic frustration due to the antiferromagnetic triangles as in kagome and pyrochlore lattices.[49,50] Thus, the OOR instability in the solid solutions is affected not only by the size of A'-site cations but also the structural frustration effects due to the mixed alkali metal ions in the intervening layers. Such a deviation from Vegard's laws is in stark contrast to a monotonous variation of Curie temperatures with Zr contents in the HIF complete solid solution system $Sr_3(Sn_{1-x}Zr_x)_2O_7$, the end members of which adopt the same OOR patterns and hence no structural frustration effects.[42]

Conclusions

In summary, DJ double-layered perovskite $Cs_{1-x}Rb_xNdNb_2O_7$ complete solid solutions were obtained by high-temperature solid-state reaction methods. The temperature-composition phase diagram was determined by combining the variable-temperature SXRD, DSC, optical SHG, and permittivity measurements. The Cs-rich samples ($x \leq 0.25$) crystalize into the polar $P2_1am$ structures at room temperature, while the Rb-rich samples ($x \geq 0.5$) adopt the *I*2*cm* structures. Ferroelectricity was demonstrated for all the compositions at room temperatures. The room-temperature remanent polarization values increase monotonously as the Rb contents increase, although the polar displacements of cations do not exhibit such a monotonous dependence on Rb contents. The Cs-rich samples undergo the thermally-induced phase transitions from the $P2_1am$ to *C*2/*m* to *P*4/*mmm* phases, while the Rb-rich samples exhibit the phase transitions pathway from the *I*2*cm* to *Cmca* to *P*4/*mmm* phases on heating. Both the polar-to-nonpolar and nonpolar-to-nonpolar phase transition temperatures for the solid solutions with intermediate compositions are lower than the interpolated values from the two end members. The deviation from a Vegard's law is likely to stem from structural

frustration effects due to the random arrangement of two types of alkali metal ions at the A' sites. This work gives insight into a role of the intervening A'-site alkali metal ions in the crystal structures and ferroelectric properties of HIF DJ double-layered perovskites.

Data availability

The data associated with this article are available in the manuscript and its ESI.†

Conflicts of interest

There are no conflicts to declare.

Acknowledgements

This research was supported by the Japan Society of the Promotion of Science (JSPS) KAKENHI Grants (No. JP17K19172, JP18H01892, JP21K19027, JP21H05568, JP21H04619, and JP23H01869), the Murata Science Foundation, and Collaborative Research Project of Laboratory for Materials and Structures, Institute of Innovative Research, Tokyo Institute of Technology. Z. L. was financially supported by Chinese Scholarship Council (No. 202008320325). S. Y. and V. G. were supported by the National Science Foundation Grant number NSF DMR-2210933. The synchrotron radiation experiments were performed at the BL02B2 of SPring-8 with the approval of the Japan Synchrotron Radiation Research Institute (JASRI) (Proposal No. 2018A1152, 2018B1227, 2023A1875, and 2023B2047).

References

1 J.-N. Li, X.-H. Li, W.-D. Yao, W. Liu and S.-P. Guo, *Chem. Commun.*, 2021, **57**, 5175–5178.
2 Z.-T. Lu, W.-J. Fan, Z.-Q. Wang, N. Gu, Z.-H. Yue, H.-G. Xue and S.-P. Guo, *Inorg. Chem.*, 2020, **59**, 7905–7909.
3 M. B. Smith, K. Page, T. Siegrist, P. L. Redmond, E. C. Walter, R. Seshadri, L. E. Brus and M. L. Steigerwald, *J. Am. Chem. Soc.*, 2008, **130**, 6955–6963.
4 S. Yoshida, H. Akamatsu, R. Tsuji, O. Hernandez, H. Padmanabhan, A. Sen Gupta, A. S. Gibbs, K. Mibu, S. Murai, J. M. Rondinelli, V. Gopalan, K. Tanaka and K. Fujita, *J. Am. Chem. Soc.*, 2018, **140**, 15690–15700.
5 T. Weigel, C. Ludt, T. Leisegang, E. Mehner, S. Jachalke, H. Stöcker, T. Doert, D. C. Meyer and M. Zschornak, *Phys. Rev. B*, 2023, **108**, 054105.
6 L. N. Kholodkovskaya, V. A. Dolgikh and B. A. Popovkin, *J. Solid State Chem.*, 1995, **116**, 406–408.
7 S. Trolier-McKinstry, S. Zhang, A. J. Bell and X. Tan, *Annu. Rev. Mater. Res.*, 2018, **48**, 191–217.
8 F. Gao, L. Cheng, R. Hong, J. Liu, C. Wang and C. Tian, *Ceram. Int.*, 2009, **35**, 1719–1723.
9 L. Qi, S. Ruan and Y.-J. Zeng, *Adv. Mater.*, 2021, **33**, 2005098.
10 Z. Guan, H. Hu, X. Shen, P. Xiang, N. Zhong, J. Chu and C. Duan, *Adv. Electron. Mater.*, 2020, **6**, 1900818.
11 A. S. Gupta, H. Akamatsu, M. E. Strayer, S. Lei, T. Kuge, K. Fujita, C. dela Cruz, A. Togo, I. Tanaka, K. Tanaka, T. E. Mallouk and V. Gopalan, *Adv. Electron. Mater.*, 2016, **2**, 1500196.
12 R. Guo, L. You, Y. Zhou, Z. Shiuh Lim, X. Zou, L. Chen, R. Ramesh and J. Wang, *Nat. Commun.*, 2013, **4**, 1990.
13 H. Lei, D. Hardy and F. Gao, *Adv. Funct. Mater.*, 2021, **31**, 2105898.
14 L. Li, P. A. Salvador and G. S. Rohrer, *Nanoscale*, 2014, **6**, 24–42.
15 C. Ederer and N. A. Spaldin, *Phys. Rev. B: Condens. Matter Mater. Phys.*, 2006, **74**, 020401.
16 W. Gong, J.-F. Li, X. Chu, Z. Gui and L. Li, *Acta Mater.*, 2004, **52**, 2787–2793.
17 C.-L. Jia, K. W. Urban, M. Alexe, D. Hesse and I. Vrejoiu, *Science*, 2011, **331**, 1420–1423.
18 G. Chen, K. Zou, Y. Yu, Y. Zhang, Q. Zhang, Y. Lu and Y. He, *Ceram. Int.*, 2020, **46**, 4148–4153.
19 M. Ichiki, H. Furue, T. Kobayashi, R. Maeda, Y. Morikawa, T. Nakada and K. Nonaka, *Appl. Phys. Lett.*, 2005, **87**, 222903.
20 A. Sen Gupta, H. Akamatsu, F. G. Brown, M. A. T. Nguyen, M. E. Strayer, S. Lapidus, S. Yoshida, K. Fujita, K. Tanaka, I. Tanaka, T. E. Mallouk and V. Gopalan, *Chem. Mater.*, 2017, **29**, 656–665.
21 N. A. Benedek and C. J. Fennie, *Phys. Rev. Lett.*, 2011, **106**, 107204.
22 E. Bousquet, M. Dawber, N. Stucki, C. Lichtensteiger, P. Hermet, S. Gariglio, J.-M. Triscone and P. Ghosez, *Nature*, 2008, **452**, 732–736.
23 N. A. Benedek, *Inorg. Chem.*, 2014, **53**, 3769–3777.
24 N. A. Benedek and M. A. Hayward, *Annu. Rev. Mater. Res.*, 2022, **52**, 331–355.
25 J. M. Rondinelli and C. J. Fennie, *Adv. Mater.*, 2012, **24**, 1918.
26 X. Q. Liu, J. W. Wu, X. X. Shi, H. J. Zhao, H. Y. Zhou, R. H. Qiu, W. Q. Zhang and X. M. Chen, *Appl. Phys. Lett.*, 2015, **106**, 202903.
27 S. Yoshida, K. Fujita, H. Akamatsu, O. Hernandez, A. Sen Gupta, F. G. Brown, H. Padmanabhan, A. S. Gibbs, T. Kuge, R. Tsuji, S. Murai, J. M. Rondinelli, V. Gopalan and K. Tanaka, *Adv. Funct. Mater.*, 2018, **28**, 1801856.
28 X. Q. Liu, J. J. Lu, B. H. Chen, B. H. Zhang and X. M. Chen, *J. Appl. Phys.*, 2019, **125**, 114105.
29 X. Xu, Y. Wang, F.-T. Huang, K. Du, E. A. Nowadnick and S.-W. Cheong, *Adv. Funct. Mater.*, 2020, **30**, 2003623.
30 K. A. Smith, S. P. Ramkumar, N. C. Harms, A. J. Clune, X. Xu, S.-W. Cheong, Z. Liu, E. A. Nowadnick and J. L. Musfeldt, *Phys. Rev. B*, 2021, **104**, 064106.
31 A. M. Glazer, *Acta Crystallogr., Sect. B*, 1972, **28**, 3384–3392.
32 M. W. Lufaso and P. M. Woodward, *Acta Crystallogr., Sect. B:Struct. Sci.*, 2004, **60**, 10–20.
33 N. A. Benedek and C. J. Fennie, *J. Phys. Chem. C*, 2013, **117**, 13339–13349.
34 S. Mallick, A. S. Gibbs, W. Zhang, P. S. Halasyamani, N. A. Benedek and M. A. Hayward, *Chem. Mater.*, 2020, **32**, 7965–7972.

35 T. Zhu, A. S. Gibbs, N. A. Benedek and M. A. Hayward, *Chem. Mater.*, 2020, **32**, 4340–4346.
36 C. Chen, H. Ning, S. Lepadatu, M. Cain, H. Yan and M. J. Reece, *J. Mater. Chem. C*, 2015, **3**, 19–22.
37 S. Pal, R. Nagarajan and S. Uma, *Chem. Mater.*, 2023, **35**, 1249–1258.
38 Z. Yan, D. Zhang, X. Zhou, M. Zhang, Y. Yue, L. Zhang, G. Xue, H. Luo, I. Abrahams and H. Yan, *Acta Mater.*, 2020, **200**, 971–979.
39 M. E. Strayer, A. S. Gupta, H. Akamatsu, S. Lei, N. A. Benedek, V. Gopalan and T. E. Mallouk, *Adv. Funct. Mater.*, 2016, **26**, 1930–1937.
40 B.-W. Li, M. Osada, T. C. Ozawa and T. Sasaki, *Chem. Mater.*, 2012, **24**, 3111–3113.
41 T. Zhu, T. Cohen, A. S. Gibbs, W. Zhang, P. S. Halasyamani, M. A. Hayward and N. A. Benedek, *Chem. Mater.*, 2017, **29**, 9489–9497.
42 Q. S. Chen, B. H. Zhang, B. H. Chen, X. Q. Liu and X. M. Chen, *J. Appl. Phys.*, 2022, **131**, 184102.
43 S. Kawaguchi, M. Takemoto, K. Osaka, E. Nishibori, C. Moriyoshi, Y. Kubota, Y. Kuroiwa and K. Sugimoto, *Rev. Sci. Instrum.*, 2017, **88**, 085111.
44 J. Rodríguez-Carvajal, *Phys. B*, 1993, **192**, 55–69.
45 K. Momma and F. Izumi, *J. Appl. Cryst.*, 2008, **41**, 653–658.
46 N. E. Brese and M. O'Keeffe, *Acta. Crystallogr., Sect. B:Struct. Sci.*, 1991, **47**, 192–197.
47 S. Asaki, H. Akamatsu, G. Hasegawa, T. Abe, Y. Nakahira, S. Yoshida, C. Moriyoshi and K. Hayashi, *Jpn. J. Appl. Phys.*, 2020, **59**, SPPC04.
48 N. A. Benedek, J. M. Rondinelli, H. Djani, P. Ghosez and P. Lightfoot, *Dalton Trans.*, 2015, **44**, 10543–10558.
49 A. P. Ramirez, *Annu. Rev. Mater. Res.*, 1994, **24**, 453–480.
50 J. A. Mydosh, *Spin Glasses: An Experimental Introduction*, CRC Press, London, 2014.